Lab on a Chip

PAPER

View Article Online
View Journal | View Issue

Cite this: *Lab Chip*, 2025, **25**, 5894

Stimulus-induced mechanical compaction of biological polymer networks *via* smart hydrogel microstructures

Vicente Salas-Quiroz, [ab] Katharina Esch [ab] and Katja Zieske *[ab]

The remodeling of the extracellular matrix by mechanical forces plays a crucial role in organizing cellular microenvironments. To study these mechanical perturbations, various methods have been developed to modify the cellular microenvironment and to apply controlled forces. However, most existing approaches rely either on instruments that cannot be integrated into lab-on-chip systems or on small probes with limited spatiotemporal precision. In this work, a lab-on-chip system enables spatially and temporally controlled mechanical perturbations of biological polymer networks. First, thermoresponsive hydrogel microstructures within flow chambers are fabricated and their material composition and photopolymerization parameters are optimized. Second, the expansion of hydrogel microstructures upon a temporally controlled temperature stimulus results in compression of Matrigel and collagen networks. Following compression, Matrigel is plastically deformed, whereas the collagen network relaxes elastically. Finally, the compression of collagen networks is spatially modulated by integrating hydrogel structures responsive to light stimuli and demonstrated to be cell compatible. By mimicking the pushing forces of cells that remodel biological polymer networks, the presented smart hydrogel microstructures provide a versatile system for future studies on extracellular matrix remodeling and the effects of mechanical forces on cellular microenvironments in both physiological and pathological contexts.

Received 14th May 2025,
Accepted 22nd September 2025

DOI: 10.1039/d5lc00477b

rsc.li/loc

Introduction

Mechanical remodeling of the extracellular microenvironment plays a crucial role in biological processes such as maintaining normal homeostasis,[1] morphogenesis,[2] and wound healing.[3] However, mimicking such mechanical deformations in reconstituted microenvironments remains a challenge. Therefore, the development of assays capable of mechanically perturbing biological polymer networks is highly desirable for elucidating how mechanical deformations contribute to normal tissue development and pathological conditions.

Despite progress in optical methods such as multiphoton microscopy[4] and Brillouin measurements,[5] studying the influence of mechanical perturbations in multicellular systems systematically remains challenging,[6] because living tissues are highly complex due to the large number of different cell types and their numerous interactions with extracellular components. To systematically investigate how mechanical perturbations affect biological processes, bottom-up approaches provide a promising strategy.[7] Three-dimensional model tissues, such as organoids[8] and cancer spheroids,[9] mimic specific properties of tissues or organs and represent more controlled multicellular systems. In addition, lab-on-chip systems are being developed to provide highly controlled fluid media compositions for culturing these model tissues and enabling parallelization.[10]

However, how mechanical remodeling of microenvironments within lab-on-chip systems impacts the function and organization of three-dimensional model tissues remains poorly understood. One limitation of current techniques is the lack of suitable techniques to generate mechanical perturbation in biological polymer networks within lab-on-chip systems. Existing techniques for applying mechanical forces on cellular systems include atomic force microscopy, microneedles,[11] and confinement force microscopy.[12] However, these techniques are difficult to integrate into enclosed microfluidic lab-on-chip systems due to their large size and the need for direct contact with the samples. Alternative techniques, such as magnetic and optical tweezers,[13] do not require direct contact with the sample and instead apply mechanical perturbation using small probes, which are guided by light or magnetic fields. However, these probes are typically spherical and the shape variations are limited. In addition, the number of

[a] *Molecular Biophysics and Living Matter, Max Planck Institute for the Science of Light, Erlangen, Germany. E-mail: katja.zieske@mpl.mpg.de*
[b] *Department of Physics, Friedrich-Alexander Universität Erlangen Nürnberg, Erlangen, Germany*

independently controllable probes is often limited. Thus, the requirement arises for developing new microscale tools for mechanical perturbations of biological polymer networks that are compatible with lab-on-chip systems.

Smart hydrogels are powerful materials for microscale actuation and have been polymerized into diverse geometries.[14] These hydrogels are composed of responsive polymers that change their structure in response to specific stimuli such as pH, light, or temperature.[15] Thereby, a smart hydrogel contracts or expands. We hypothesized that these actuations can be exploited to mechanically perturb biological polymer networks. While smart hydrogels have primarily been used in engineering sciences and studied for drug delivery and surface coating applications,[16] their use in biomechanical applications remains limited. So far, light-sensitive hydrogel microactuators integrated with non-responsive components show promise for exerting forces on cells.[17] In addition, smart hydrogel beads have been used to actuate cellular environments,[18] and fillings of smart hydrogel have been used to actuate microfabricated pillars, which mechanically stimulated individual pillar-interacting cells.[19] Moreover, light-responsive hydrogel sheets with grooves and coated with collagen have been employed to mechanically perturb cells plated on these surfaces.[20] However, smart hydrogel microstructures with defined geometries have not yet been implemented for perturbation of biopolymer networks in lab-on-chip flow chambers.

To polymerize pre-gel solutions into defined geometrical microstructures various methods have been implemented. Standard photolithography enables the fabrication of hydrogel microstructures with defined two-dimensional geometries. However, this approach typically requires a photomask, limiting the geometries of hydrogel microstructures to the predefined features on the mask.[21] Maskless methods for photopolymerization of hydrogel structures include two-photon lithography or light pattern modulation using a digital mirror device (DMD). Two-photon lithography allows for the fabrication of three-dimensional hydrogel shapes. However, this method is limited by its low speed and high cost.[22] DMD-based devices, in contrast, define hydrogel microstructures in two-dimension. Compared to two-photon-lithography, their advantages include faster polymerization of multiple hydrogel structures and lower cost.[23,24] Notably, many scientific questions related to perturbation, system development, and observation of minimal model tissues can be addressed in two-dimensionally defined systems.[25] Thus, DMD-based polymerization of hydrogels represents a promising approach, integrating the flexibility of user-defined two-dimensional shapes with efficient fabrication times.

Here, we present an approach to remodel biological polymer networks within flow chambers with a high spatiotemporal control using smart hydrogel microstructures stimulated by temperature and light. We optimized polymerization parameters for generating hydrogel microstructures in flow chambers and demonstrated that the stimulated expansion of hydrogel microstructures leads to compaction of biological polymer networks, such as collagen and Matrigel. Moreover, we demonstrate that the mechanical remodeling of biological polymer networks smart hydrogel microstructures can be controlled in space and time, while remaining cell compatible.

Results and discussion

To exert forces on biological polymer networks, we established a workflow for fabricating thermoresponsive hydrogel microstructures *via* mask-less photoprinting and optimized the printing parameters. The pre-gel solution was composed of two photoinitiators – Irgacure 2959, which enables free radical polymerization,[26] and 4-benzoybenzyl-trimethylammonium chloride – along with the crosslinker *N*, *N*′-methylenbisacrylamid (MBAm), the non-responsive 4-arm poly(ethylene glycol)-acrylate (4-arm-PEG) and the thermoresponsive polymer poly(*N*-isopropylacrylamide) (NiPAAm). Previously, we demonstrated that a pre-gel solution containing these components adheres to glass surfaces and expands upon temperature stimuli.[27] The liquid pre-gel mixture was injected into a custom-made flow chamber. To photopolymerize the precursor solution into defined microstructures, patterns of UV light were projected onto the sample using a digital mirror device (PRIMO, Alvéole) (Fig. 2a). By generating circular and rectangular shapes, we confirmed that different custom-defined microstructure geometries could be fabricated (Fig. 1Ai–vi). Compared to our previous study, where photomasks were applied,[27] the current setup allows for the fabrication of hydrogel microstructures with any custom-defined 2D geometry. In addition, illumination times can be controlled *via* the corresponding software to achieve controlled illumination doses.

After polymerization of the hydrogel microstructures using the digital mirror device, the thermoresponsiveness was confirmed by heating and cooling the hydrogel microstructures within an incubator chamber. To visualize hydrogel boundaries, a fluorescent probe was used that did not penetrate the hydrogel structures. Laser scanning confocal imaging was used to acquire *z*-stacks and visualize the boundaries of the hydrogel structures (Fig. 1Avi), that were easily distinguishable from their environment (Fig. 1B). When the temperature was increased to 46 °C, cylindrical hydrogel microstructures shrank to approximately 31 ± 5% of their original radius at room temperature (24 °C). This contraction was reversible upon cooling (Fig. 1B).

The volume phase transition temperature (VPTT) for NiPAAm hydrogels has been determined to be around 33 °C.[28,29] To quantitatively analyze the VPTT of our hydrogel microstructures and determine the size changes as a function of temperature, we varied the temperature in increments of two degrees between 24 and 46 °C (Fig. 1C). The data for cooling and heating cycles were fitted with a sigmoidal curve, respectively. Our data verified the presence

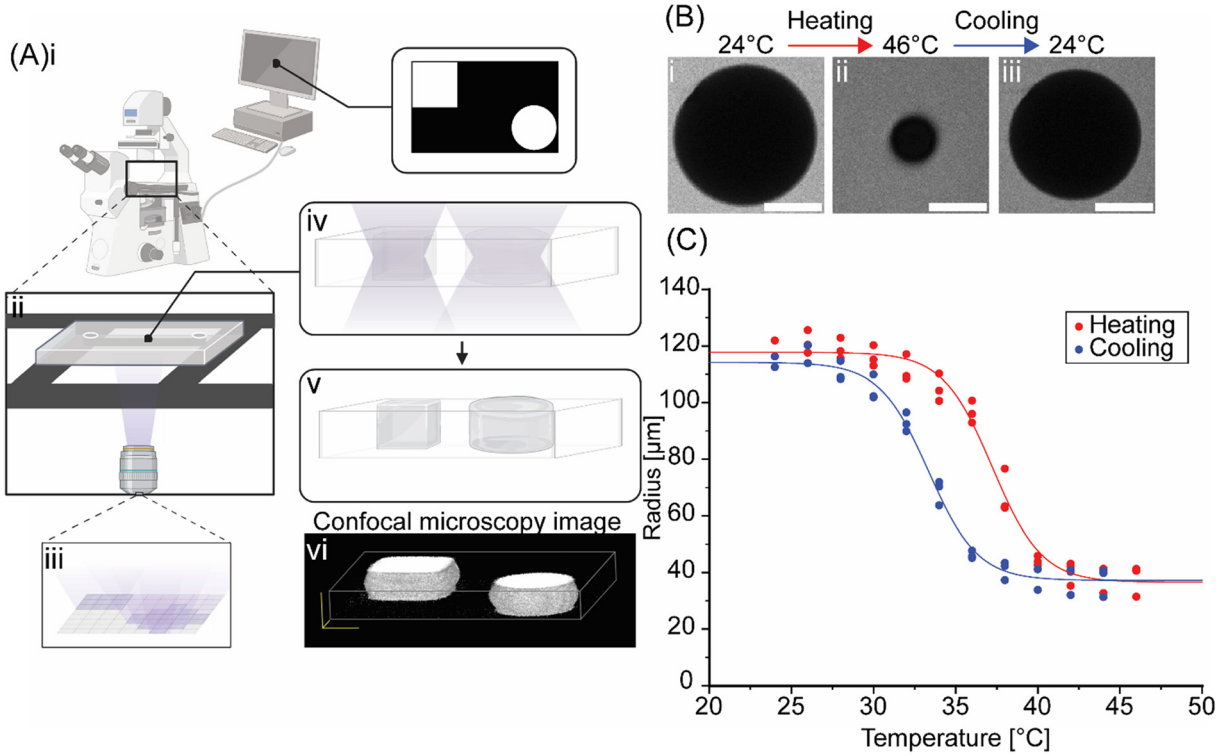

Fig. 1 Workflow for mask-less photopolymerization of thermoresponsive hydrogel microstructures. (A) Digital images with custom-designed patterns were interpreted by the software of a digital mirror device (PRIMO) connected to an inverted microscope (i). The hydrogel precursor solution within a flow chamber (ii) was exposed to the corresponding UV light patterns (iii and iv), resulting in the photopolymerization of hydrogel microstructures into defined shapes (v). (vi) A three-dimensional visualization of hydrogel microstructures reconstituted from *z*-stack images acquired using a laser-scanning confocal microscope (created with **https://Biorender.com**). (B) Confocal microscopy images of a cylindrical hydrogel microstructure at room temperature (24 °C) (i), after heating to 46 °C (ii), and after re-cooling to room temperature (iii). The flow chamber was supplemented with PLL-*g*-PEG/FITC (1 mg mL^{-1}). (C) The swelling and shrinkage of hydrogel microstructures was quantified during heating (red) and cooling (blue) by measuring the radius. The sigmoidal curve was fitted using the dose–response equation. Heating curve: $y = 36.6 + (117.8 - 36.6)/(1 + 10^{((37.2 - x) \times -0.3)})$; cooling curve: $y = 37.2 + (114.2 - 37.2)/(1 + 10^{((33.4 - x) \times -0.3)})$. Independent samples: $n = 3$. Scale bars: 100 μm.

of thermal hysteresis, which has been reported previously.[30,31] The VPTT of our hydrogel microstructures during the heating cycle was 37.2 ± 2 °C. During the cooling cycle, the VPTT was 33.3 ± 2 °C. These VPTTs have advantages for future cellular applications, as size changes can be triggered within the physiological relevant temperature range.[32,33] The expansion of these fabricated hydrogel microstructures therefore provides an intriguing opportunity for applying pushing forces in biological contexts within lab-on-chip chambers.

Next, we determined the optimal illumination dose and material composition for microstructure polymerization and controlled gel expansion. Previously, we reported a hydrogel mixture for generating adherend thermoresponsive microstructures on glass,[27] which consisted of a thermoresponsive pre-gel fraction including NiPAAm and a non-responsive material fraction, containing 4-arm PEG. Here, we systematically studied how varying the ratio of the NiPAAm containing fraction (0, 20, 50, 62, 75, 87, and 100% v/v) and the polymerization dose affected the formation of hydrogel microstructures (Fig. 2A). Thereby, we observed three major outcomes. First, at low UV doses and low fractions of the NiPAAm containing pre-gel solution, the hydrogel did not polymerize. Similarly, at a very low UV dose of 50 mJ mm^{-2}, even high NiPAAm-containing formulations did not polymerize (Fig. 2A and B bottom). Second, at medium UV doses and medium-to-high fractions of the NiPAAm containing pre-gel solution, the hydrogel polymerized into geometrically well-defined and thermoresponsive microstructures (Fig. 2A and B, top). Finally, at high UV doses and high fractions of the NiPAAm containing pre-gel solution, the resulting microstructures exhibited aberrant geometries (Fig. 2A and B, middle).

Next, we quantified the thermoresponsiveness of the geometrically well-defined hydrogel microstructures by measuring their radius in the expanded and contracted states. First, we measured the dependence of the microstructure radii on UV dose, using a fixed fraction of the NiPAAm containing pre-gel solution of 75% (w/v). For UV doses between 200 mJ mm^{-2} and 500 mJ mm^{-2}, the hydrogel microstructures exhibited well-defined geometries and displayed clear temperature responsiveness (Fig. 2C). The radius of the hydrogel microstructures increased with increasing UV doses. This trend is likely caused by prolonged light exposure resulting in polymerization beyond the intended pattern areas.

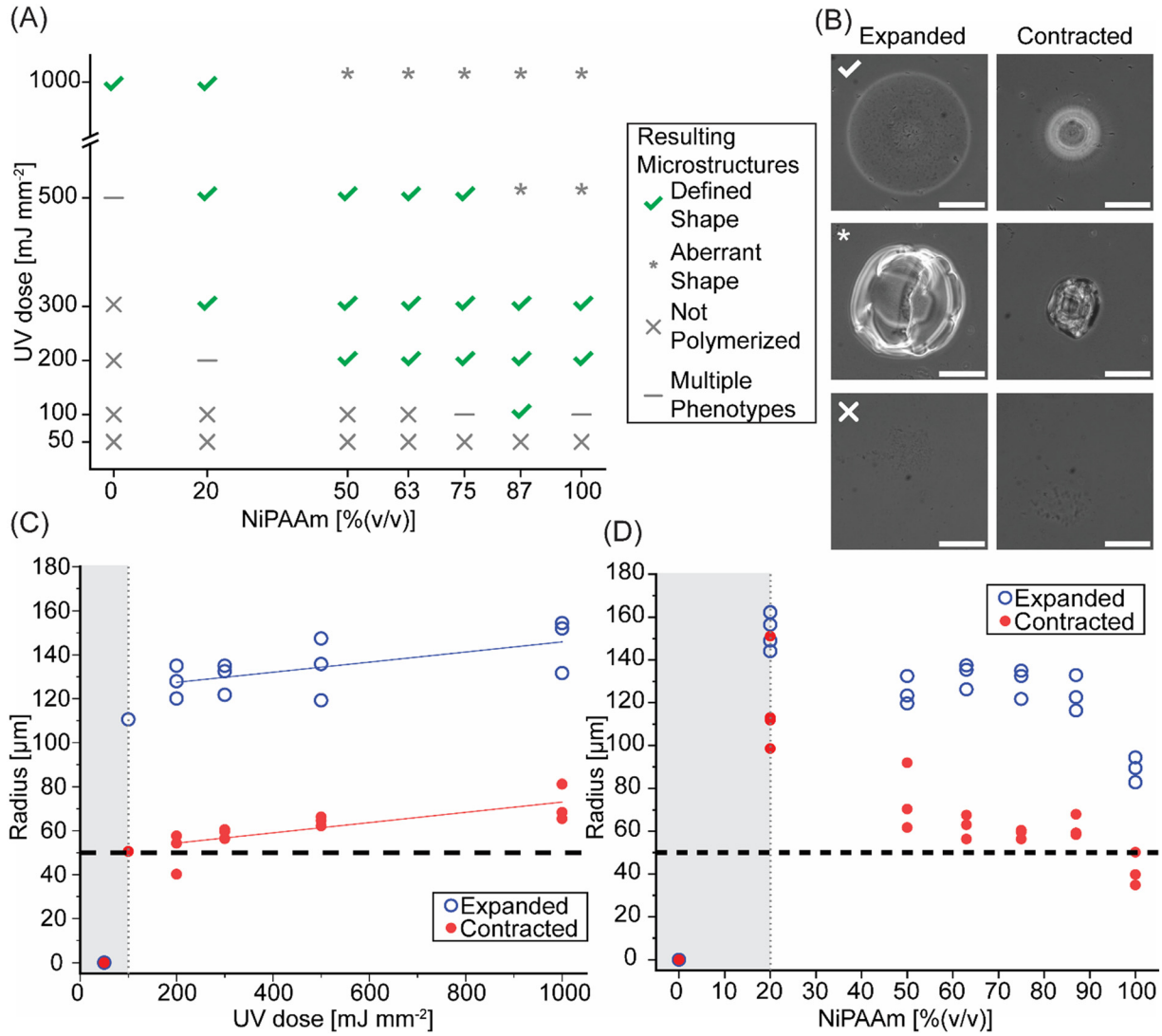

Fig. 2 Optimization of illumination settings and material composition for generating thermoresponsive hydrogel microstructures. (A) Hydrogel compositions with varying ratios of the NiPAAm-containing pre-gel solution (0% to 100%) were exposed to UV light doses ranging from 50 mJ mm^{-2} to 1000 mJ mm^{-2}. Depending on the specific combination of parameters, different phenotypes were observed: hydrogel microstructures did not polymerize (X), well-defined hydrogel microstructures that successfully polymerize (checkmark), multiple phenotypes appeared (-), and hydrogel microstructures with aberrant geometries polymerized (*). (B) Representative images of the various hydrogel microstructure phenotypes in their expanded state at room temperature and their contracted state at 60 °C. Scale bars: 100 µm. (C) The radii of photopolymerized microstructures were measured as a function of UV dose. The fraction of NiPAAm-containing pre-gel solution was held constant at 75% (v/v). The shaded grey area represents parameter combinations that did not result in the polymerization of defined structures. Data were fitted using the following functions: expanded state: $y = 122.84 + 0.02 \times x$; contracted state: $y = 49.69 + 0.02 \times x$. (D) Radii of photopolymerized hydrogel microstructures were measured as a function of the fraction of NiPAAm-containing precursor solution. The UV dose was held constant at 300 mJ mm^2. The shaded grey area indicates parameter combinations that that did not result in the polymerization of well-defined structures. Independent samples for each condition (A–D): $n = 3$.

We also measured how the fraction of the NiPAAm containing pre-gel solution affected the microstructure radii while maintaining a constant UV dose of 300 mJ mm^{-2} (Fig. 2D). Without NiPAAm, no hydrogel microstructures polymerized. At low NiPAAm fractions, the resulting structures were larger than the digital templates. Geometrically defined hydrogel microstructures, which displayed clear temperature responsiveness, were observed for NiPAAm containing fractions above 50%.

Together these results establish a mask-less alternative for patterning thermoresponsive hydrogel microstructures within flow chambers. We found optimal fabrication parameters to polymerize microstructures that reflect the geometry of the custom-designed digital templates while maintaining thermoresponsiveness and adhesion to the flow chamber surface. The optimal range of fabrication parameters is represented by a UV dose of 200 mJ mm^{-2} to 500 mJ mm^{-2} and a NiPAAm containing pre-gel solution of 50% to 100% (v/v). For subsequent

experiments, we used a UV dose of 300 mJ mm^{-2} and a NiPAAm containing pre-gel solution of 75% (v/v). Under these conditions, the hydrogel microstructures exhibited controlled size changes, enabling precise application of mechanical forces to their surroundings.

Previous studies demonstrated the compaction of fibrin and collagen networks with expanding bubbles.[34,35] Compared to those studies, the polymerization of smart hydrogel microstructures offers control over the actuator shape. Thus, we explored whether expanding hydrogel microstructures could mechanically perturb biological polymer networks. Specifically, we filled the hydrogel structure containing flow chambers with Matrigel or collagen and studied whether these polymer networks are remodeled through the mechanical forces applied by stimulated hydrogel microstructures. After gelling of the biological

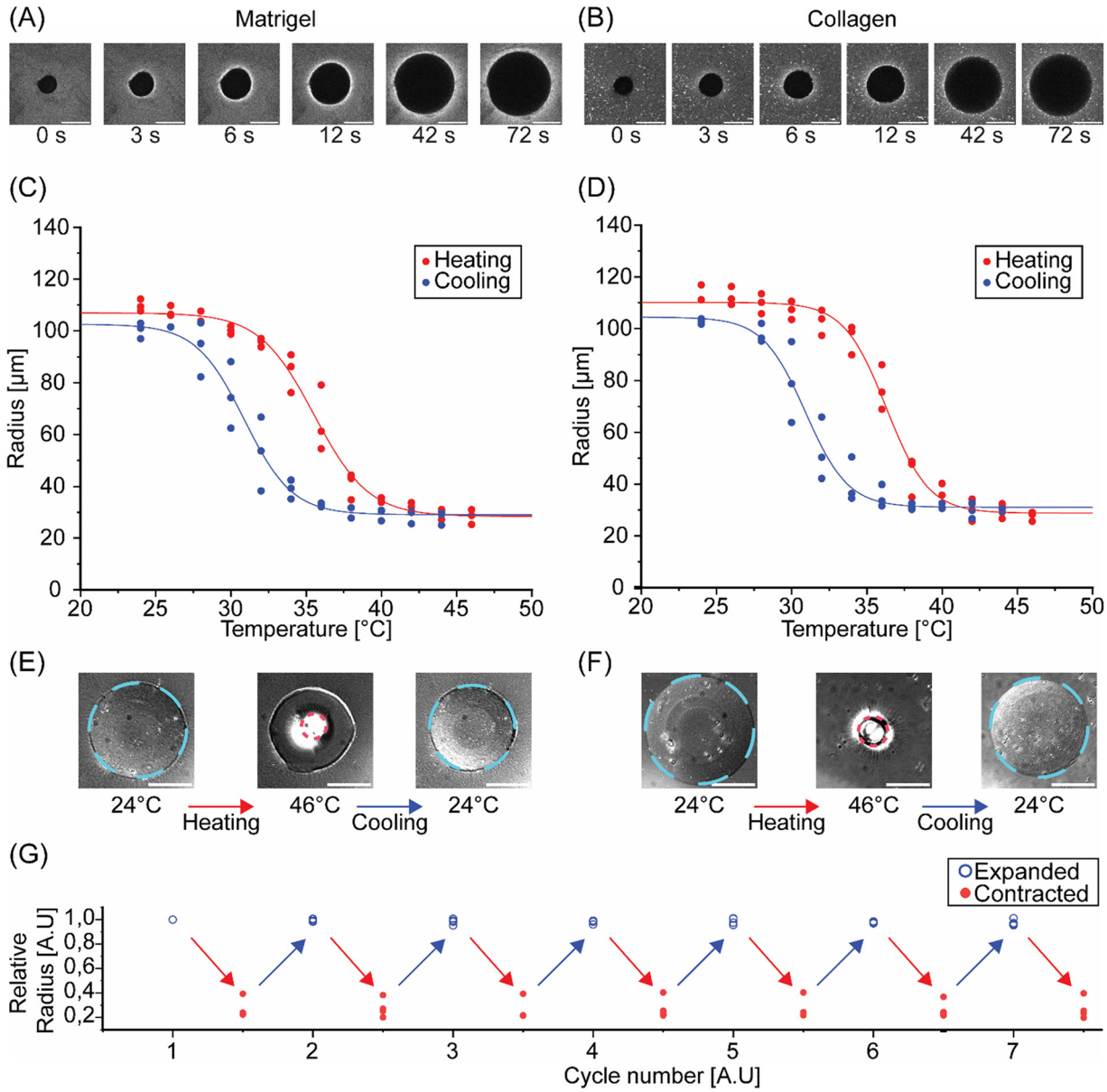

Fig. 3 Biological polymer networks are mechanically compacted by expanding hydrogel microstructures. (A) Confocal time-lapse microscopy images showing hydrogel microstructure expansion in the presence of Matrigel. To expand the hydrogel microstructure, the temperature was lowered from 37 °C to room temperature (24 °C). The Matrigel mixture was supplemented with the fluorescent probe PLL-*g*-PEG/FITC (47.6 µg mL^{-1}). (B) The same experiment was performed in the presence of collagen. (C) and (D) Quantification of the radii of cylindrical hydrogel microstructures during heating (red) and cooling (blue) in the presence of Matrigel (C) and collagen (D). Data were fitted with sigmoidal curves. Matrigel: heating curve: $y = 28.8 + (110.1 - 28.8)/(1 + 10^{((36.3 - x) \times -0.3)})$: cooling curve: $y = 31.1 + (104.4 - 31.1)/(1 + 10^{((30.9 - x) \times -0.3)})$. Collagen: heating curve: $y = 28.4 + (106.9 - 28.4)/(1 + 10^{((35.5 - x) \times -0.2)})$; cooling curve: $y = 29.1 + (102.6 - 29.1)/(1 + 10^{((30.9 - x) \times -0.3)})$. (E) and (F) Representative brightfield images showing hydrogel microstructures within Matrigel and collagen at different temperatures during the heating–cooling cycle. The dashed circle indicates the boundaries of the microstructure. (G) Quantification of multiple heating–cooling cycles demonstrating the repeatability of hydrogel structure size changes in collagen. Scale bars: 100 µm. Independent samples (A–F): $n = 3$. (G): $n \geq 3$.

polymer networks, the samples were subjected to heating and cooling cycles and imaged to study the behavior of the microstructures and the surrounding polymer networks.

First, we characterized samples containing membrane-based Matrigel, a widely utilized extracellular matrix-based material for mimicking cellular environments.[36] For visualization purposes, we supplemented the Matrigel with FITC-labeled PLL-*g*-PEG. The Matrigel was gelled within the flow chamber at 37 °C while the hydrogel microstructures were in the contracted state. Upon cooling to room temperature, the hydrogel microstructures expanded and pushed against the surrounding Matrigel. The microstructure expansion caused a compaction of the Matrigel (Fig. 3A). This result demonstrated that our microstructures generate sufficient force to mechanically remodel the gelled Matrigel network. The local compaction of Matrigel was further evidenced by the accumulation of the fluorescent probe around the rim of the hydrogel microstructure during expansion (Fig. 3A). Compared to a sample without Matrigel, the expanded hydrogel microstructures in Matrigel were slightly smaller. This size difference in aqueous solution and within Matrigel is likely caused by the mechanical resistance of the surrounding Matrigel network. After the initial expansion, the samples were heated to 46 °C and subsequently cooled to 24 °C (Fig. 3C and E) to characterize the varying radii of the hydrogel structures during temperature changes. The sigmoidal compaction and expansion dynamics of the microstructures were similar in the presence and absence of Matrigel.

Notably, during hydrogel contraction, a gap appeared between the Matrigel and the microstructure (Fig. 3E, middle panel). This suggests that Matrigel deforms plastically under mechanical perturbations imposed by expanding hydrogel structures. This observation aligns with previous studies reporting plastic remodeling of Matrigel[37–40] and demonstrates the potential of smart hydrogel microstructures as tools for generating localized, plastic deformations in Matrigel at the micron scale. *In vivo*, the plastic remodeling of extracellular polymer networks by cellular forces plays a crucial role in processes such as cancer cell invasion of basement membranes.[41]

To characterize another biological polymer network within our system, we filled the flow chambers with type I collagen, a widely studied biopolymer in biomedical and bioengineering research.[42] Similar to Matrigel, we observed compaction of the collagen network during the initial expansion of the hydrogel microstructures (Fig. 3B). However, in contrast to Matrigel, the collagen network refilled the space vacated by the contracting microstructures (Fig. 3F, middle panel). As collagen networks may partly liquify at temperatures of 46 °C (Fig. S2), we confirmed that the vacated space was also refilled at heating temperatures of 40 °C and used a temperature of 40 °C for the following experiment (Fig. 4A). The relaxation toward the vacated space may be caused by the elastic regime of collagen, which enables elastic relaxation of collagen networks up to a critical

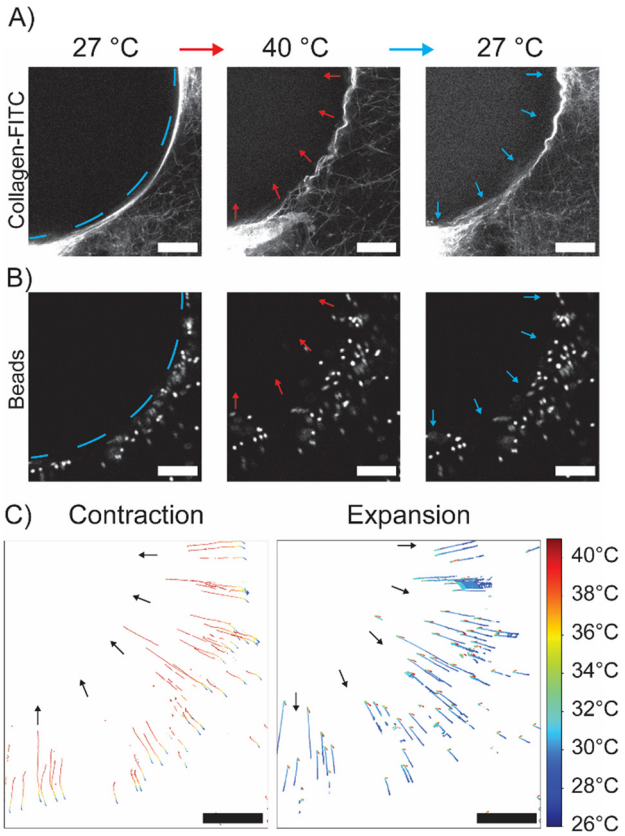

Fig. 4 Local characterization of collagen remodeling induced by the thermoresponse of hydrogel microstructures. (A) Confocal microscopy images of FITC-labeled collagen (2.5%) during heating (red arrows) and cooling (blue arrows) located near the microstructure (blue dashed line). (B) Confocal microscopy images of fluorescent beads embedded in collagen during heating and cooling near the microstructure. (C) Displacement trajectories were plotted for a beads near thermoresponsive microstructures during heating from 27 °C (blue) to 40 °C (red) and cooling back to 27 °C. Black arrows indicate the direction of movement. Scale bars: 25 μm. Independent samples: (A) n = 3, (B and C) n = 4.

strain threshold.[43,44] Beyond this threshold, strains may cause plastic deformation.[45,46] Our results suggest that the strain generated by the thermoresponsive microstructures remains below this critical threshold. Thus, our system cannot only be applied to induce pushing forces, but also to allow the relaxation of collagen networks.

We performed multiple heating–cooling cycles with collagen networks (Fig. 3G) and demonstrated that the compaction and expansion of collagen networks were reversible and reproducible. After seven heating and cooling cycles, the radii of the microstructures in both the expanded and compacted states, did not vary more than 5%. This demonstrates the long-term stability and usability of the thermoresponsive hydrogel structures as micron-scale tools for generating mechanical forces in biopolymer networks. Our assay represents a novel biomechanical approach for remodeling biopolymer networks in lab-on-chip systems. Due to the fibrillar nature of collagen,[47] which facilitates force transmission, deformations induced by the hydrogel

structures could be detected several micrometers away from the boundaries of the hydrogel structures.

To characterize the local remodeling of the collagen network induced by the thermoresponse of the microstructures (Fig. 4), we performed experiments with fluorescently labeled collagen. After contraction of the hydrogel microstructures, the local density of the fluorescently marked collagen network decreased (Fig. 4A, middle panel). A rearrangement of the collagen fibers, which filled the space vacated by the decreasing microstructure. Upon expansion of the microstructure, the local fiber density of the collagen network increased again as a result of network compaction (Fig. 4A, right panel).

To further analyze collagen network remodeling, we embeded fluorescent beads in the collagen and determined the trajectories of these beads during heating and cooling cycles (Fig. 4B). We observed that the beads moved in the direction of contraction and subsequently in the direction of expansion, demonstrating that mechanical forces were transmitted by the microstructures through the collagen network to displace the beads. Thereby, areas with large bead displacement represent regions of maximal mechanical network deformation (Fig. 4C). During contraction (Fig. 4C, left panel), the largest bead movements occurred close to the microstructure edges, with displacements exceeding 10 μm. Smaller, directed displacements were also observed up to 50 μm away from the microstructure edge, indicating that the induced forces propagate into the collagen network. Similar behavior was observed during expansion (Fig. 4C, right panel), where the beads close to the expanding microstructure were pushed and displayed the larger displacement compared to beads further away.

The threshold temperatures required to achieve substantial bead displacement differed between contraction and expansion. This difference is caused by the hysteresis during heating *vs.* cooling of the thermoresponsive microstructures (Fig. 3D). Lower temperatures were required for bead displacements during microstructure expansion as compared to contraction. Bead displacement distances were not uniform for all beads, which could result from heterogeneous force transmission within the collagen network.[48,49]

After demonstrating network compaction around microstructures in response to an external temperature stimulus, we further functionalized our hydrogel microstructures by implementing their responsiveness to light stimuli. We aimed to use light as a trigger for inducing size changes of our hydrogel microstructures for three reasons: first, light can be adjusted to a target intensity more rapidly than an incubation chamber can reach a target temperature, allowing for faster switching. Second, while an entire sample is exposed to temperature changes within an incubation chamber, a laser beam can be spatially guided, enabling localized control of hydrogel compaction and expansion. Finally, many biological samples are temperature sensitive. Using spatially controlled light patterns to stimulate localized temperature changes within the hydrogel microstructures, while minimizing heating of the surrounding biological polymer network, could expand applications to temperature-sensitive samples.

To render hydrogel microstructures light-responsive, gold nanoparticles (AuNP) have previously been integrated into hydrogels to enable plasmonic heating upon light exposure.[19,50] To determine a AuNP concentration sufficient for inducing light-dependent volume changes in our hydrogel microstructures, we systematically varied the AuNP concentration in our pre-gel solution. Pre-gel solutions containing distinct concentrations of AuNPs were patterned into square microstructures and afterwards stimulated with an LED (460 nm, 259 mW) for 3 minutes. Imaging the hydrogel microstructures before and after stimulation demonstrated that light-induced compaction was more pronounced at higher AuNP concentrations compared to low amounts of AuNP (Fig. 5A). We quantified the relative areas of the expanded and compacted state of the hydrogel microstructures for different AuNP concentrations. The data were fitted with a sigmoidal curve that exhibited an inflection point at 0.45 nM AuNPs (Fig. 5B). This result demonstrated that AuNP concentrations above 0.45 nM effectively modulate hydrogel size changes. For the following experiments, we used a concentration of 0.63 nM AuNP.

Next, we tested whether light patterns could stimulate the contraction of individual hydrogel microstructures embedded in a collagen matrix. To do this, arrays of AuNP-containing hydrogel microstructures were generated and embedded in collagen (4 mg mL^{-1}). We selectively exposed a single hydrogel microstructure to light (561 nm) using a laser scanning microscope and observed contraction of the targeted hydrogel microstructure (Fig. 5C). This size changes were observed along the entire vertical axis of the microstructure, confirming light penetration through the entire sample height (Fig. S1). The locally selective exposure of the hydrogel microstructures also provides advantages for cellular applications, because only the microstructures would be exposed to the light, while phototoxic effects are avoided in the collagen containing areas, where cells would be embedded.

The laser intensity was systematically varied and the compaction of the hydrogel was quantified. The data show a sigmoidal response, similar to temperature-dependent contraction, with higher laser intensities resulting in more pronounced compaction (Fig. 5D). These results demonstrate the controlled expansion of individual hydrogel microstructures within our flow chambers.

We further explored spatial control of our samples by selectively illuminating subregions of the microstructures (Fig. 5E). For instance, we exposed half of a square hydrogel microstructure and then a quarter of microstructure to light. We observed contraction in the illuminated regions, while the non-exposed regions did not contract. These deformations were reversible, with hydrogel microstructures

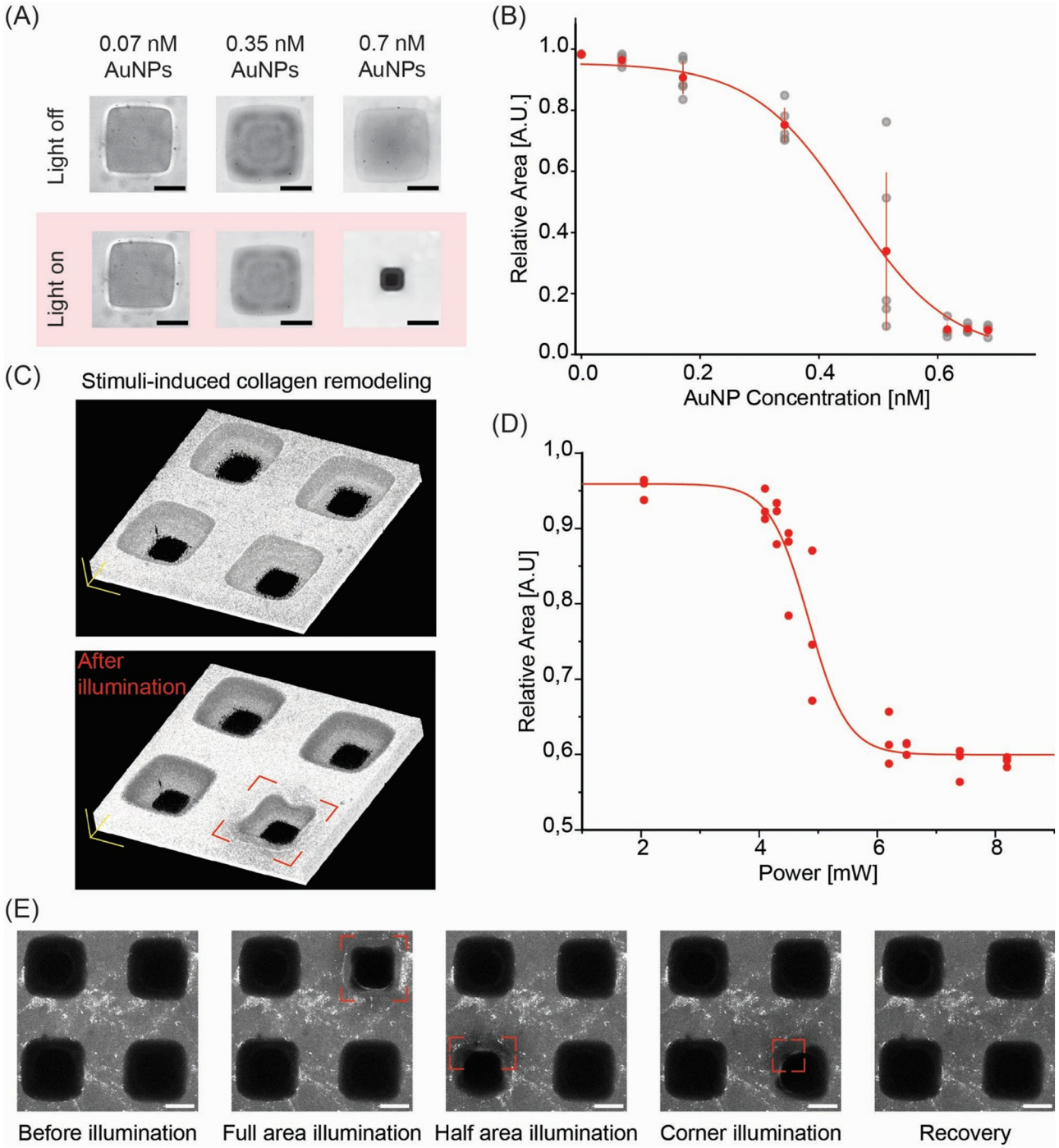

Fig. 5 Collagen deformation through light-stimulated contraction of individual hydrogel blocks. (A) Representative images of hydrogel microstructures with varying AuNP concentrations before (top) and after (bottom) light exposure (460 nm, 259 mW) for 3 minutes. (B) Relative area changes of the hydrogel microstructures as a function of AuNP concentration. Error bars indicate the standard deviation. Fit function: $y = 0.97/(1 + e^{(11.81 \times (x - 0.46)}$). (C) Three-dimensional reconstruction of collagen sample before and after illumination, acquired using a laser-scanning confocal microscope. The red square marks the illuminated hydrogel microstructure. (D) Quantification of light-driven compaction of hydrogel structures as a function of laser power. Fit function: $y = 0.6 + (1 - 0.6)/(1 + 10^{((4.8 - x) \times -1.3)})$. (E) Representative images of light-responsive hydrogel microstructures showing a microstructure before illumination, compaction upon full or subregional illumination (indicated by red squares), and recovery after cessation of light exposure. Independent samples (A and B): $n \geq 3$, (C–E): $n = 3$. Scale bars: 100 μm.

recovering their original shape and size upon cessation of illumination. The ability to control the contraction of specific subareas of the microstructures in both space and time illustrate the high level of control in hydrogel shape modulation and the resulting mechanical remodeling of biological polymer networks.

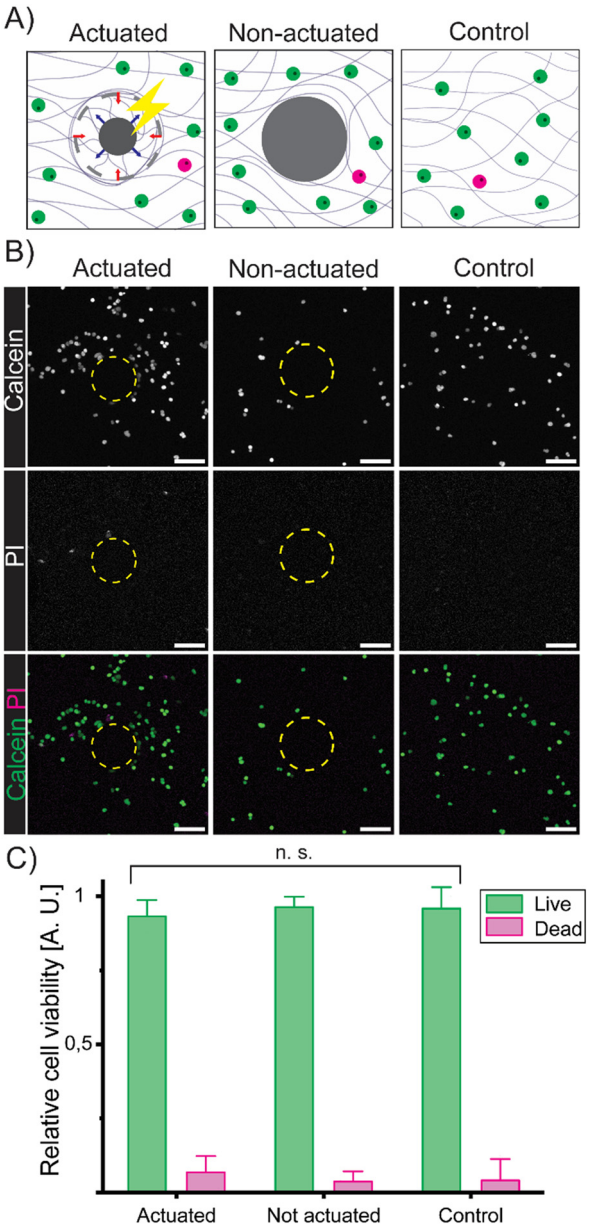

Fig. 6 Light actuated microstructures are compatible with live cells. (A) Three conditions within the sample were analyzed: cells (green and magenta) surrounding a microstructure (dashed circle), which was subjected to ten illumination cycles over 30 minutes; cells surrounding a non-actuated microstructure; and cells without a microstructure. (B) Maximum intensity projection of confocal images showing cells labeled with calcein-AM (green) and propidium iodide (PI) (magenta) after ten illumination cycles. The microstructures are indicated with yellow dashed lines. (C) Quantification of live and dead cells after ten illumination cycles. Data are shown as mean and SEM and analyzed by one-way ANOVA (p = 0.77). Scale bars: 100 μm. Independent biological samples (B and C): n = 3. Cells analyzed: n = 496.

Finally, the compatibility of our device with living cells was confirmed using a life-dead-staining assay. For this, Madin–Darby canine kidney (MDCK-II) cells were embedded in collagen and imaged in flow chambers containing light-responsive microstructures (Fig. 6A). Cells close to a microstructure (Fig. 6A and B, left panel), which was subjected to ten actuation cycles (40 seconds illumination followed by 2:20 minutes of recovery), did not differ detectably from control conditions (Fig. 6A and B, middle and right panel). Quantification of live and dead cells after ten actuation cycles confirmed that neither light activation nor the cultivation of cells in the presence of the microstructures caused significant cell death (Fig. 6C). In summary our lab-on-chip system supports cell viability, and enables the application of forces to polymer networks and cells.

Experimental

Reagents for thermoresponsive hydrogel

The thermoresponsive fraction of the pre-gel solution was composed of 4.3 M poly(*N*-isopropylacrylamide) (NiPAAm) (Sigma Aldrich), 12 mM photoinitiator 2-hydroxy-4′-(2-hydroxyethoxy)-2-methylpropiophenone (Irgacure 2959) (Sigma Aldrich), and 15 mM crosslinker *N*,*N*′-methylenbisacrylamid (MBAm) (Thermo Scientific). NiPAAm and Irgacure 2959 were dissolved in ethanol. MBAm was dissolved in ultrapure water. The nonresponsive fraction of the pre-gel solution was composed of 4-arm poly (ethylene glycol)-acrylate (4-arm PEG) (MW10K, Laysan Bio Inc.) and the photoinitiator 4-benzoybenzyl-trimethylammonium chloride (BOC Sciences). 4-arm PEG was dissolved in ultrapure water at stock concentration of 20% (w/v). 4-Benzoybenzyl-trimethylammonium chloride was dissolved in ethanol at a stock concentration of 100 mM. The stock solutions of 4-arm PEG, photoinitiator and water were mixed at a 1 : 2 : 1 ratio. The thermoresponsive and nonresponsive pre-gel solutions were mixed at various concentrations as described in the main text.

Preparation of gold nanoparticles and light responsive hydrogel

The synthesis and coating of gold nanoparticles (AuNPs) followed the citrate reduction method.[50] Briefly, gold(III) chloride hydrate (Sigma-Aldrich) was dissolved in ultra-pure water at a concentration of 1.2 mM in a piranha-cleaned Erlenmeyer flask. The solution was stirred and heated to 100 °C. A solution of 170 mM sodium citrate tribasic dihydrate (Sigma-Aldrich) in ultra-pure water was added to the gold(III) chloride hydrate solution to a final concentration of 4 mM. The mixture was continuously stirred at 100 °C for 30 minutes, whereby the color of the solution changed from pale yellow to dark red. The mixture was then cooled to room temperature.

To coat the AuNPs, 116 mM PEG_{800}-SH (Sigma-Aldrich) in water was mixed with the AuNP solution at a 0.32 : 1 ratio and incubated at room temperature for 1 hour. The mixture was centrifuged at 21 000g for 15 minutes and washed with ultra-pure water. This washing step was repeated twice. Subsequently, the AuNP sediment (50 μl; original volume: 1

mL) was collected and further concentrated by centrifugation. AuNPs in water were two-fold concentrated. To obtain AuNPs in ethanol, the nanoparticles were washed two times with ethanol and concentrated 16-fold.

For the preparation of the non-responsive pre-gel solution, a 20% 4-arm-PEG-acrylate solution was mixed with 4-benzoybenzyl-trimethylammonium chloride (100 mM), AuNPs (in water) and ultra-pure water at a ratio of 1 : 2 : 1. The light responsive pre-gel solution was composed of 4.3 M NiPAAm dissolved in the AuNP (in ethanol) solution, 12 mM Irgacure 2959, and 15 mM MBAm. To obtain the final light-sensitive hydrogel mixture, the responsive and non-responsive pre-gel solutions containing AuNPs were combined at a 3 : 1 ratio. Pre-gel solutions with lower AuNP concentrations were prepared by mixing pre-gel solutions with and without AuNPs in varying ratios (Fig. 5A and B).

Flow chambers and temperature control

To fabricate flow chambers, two strips of Parafilm were used as spacers between two glass coverslips (22 mm × 40 mm and 22 mm × 22 mm). The assembly was heated on a hot plate at 200 °C for 1 minute until the Parafilm melted. Pressure was applied with tweezers to achieve a channel height of approximately 0.1 mm.

For temperature control, a stage top incubator (Ibidi) was used. The incubator temperature was adjustable with an accuracy of ±2 °C, and stability of the temperature was verified using a temperature sensor positioned in the center of the incubator. Alternatively, the flow chamber samples were heated by placing a glass-bottom petri dish (Ibidi) filled with water at 60 °C (Fig. 2) or 46 °C (Fig. 3G) on top of the flow chamber.

To confirm that repeated heating and cooling cycles with temperatures up to 46 °C support collagen network integrity, polymerized collagen in 0.2 mL tubes was incubated at 37 °C, 39.4 °C, 42 °C, 45.1 °C, 47.3 °C, 48.9 °C and 50 °C, using a thermocycler and pictures acquired (Fig. S2).

Lithographic fabrication of hydrogel structures

Hydrogel microstructures were fabricated *via* maskless photolithography with a PRIMO device and Leonardo software (Alvéole, France). The PRIMO device was mounted on an inverted microscope (Nikon TI-E, Nikon Instruments) and projected patterns of ultraviolet light (wavelength: 375 nm) onto the flow chamber. Flow chambers were loaded with thermoresponsive or light-responsive hydrogel pre-gel mixtures (15 µl) and exposed to UV light patterns, while the central plane of the flow chamber was positioned in the focal plane. After exposure to UV light, the flow chambers were rinsed with ultrapure water (100 µl) and were used the same day.

Sample preparation for fluorescent imaging and experiments with biopolymers

For imaging hydrogel structures in the presence of a fluorescent solution during temperature modulation experiments, the water was removed, and the flow chambers were filled with of PLL-*g*-PEG/FITC at 1 mg mL^{-1} (SuSoS) (15 µl). Both ends of the flow chamber were sealed with nail polish.

For experiments of hydrogel microstructures in Matrigel (Basement Membrane Matrix, Corning) or collagen (type I, rat tail, Ibidi), water within the flow chamber was removed at 45 °C and the chamber was cooled before filling with Matrigel (15 µl) containing PLL-*g*-PEG/FITC (47.6 µg mL^{-1}) or a collagen solution. The collagen solution contained 4 mg mL^{-1} collagen, 47.6 µg mL^{-1} PLL-*g*-PEG/FITC 100 mM HEPES (VWR Chemicals) 3.7 g L^{-1} sodium bicarbonate (pH = 9.5, adjusted with sodium hydroxide), and ultrapure water. For fiber visualization, the sample contained 3.9 mg mL^{-1} collagen and 0.02 mg mL^{-1} collagen FITC (Sigma-Aldrich), 100 mM HEPES (VWR Chemicals), 3.7 g L^{-1} sodium bicarbonate and ultrapure water. For beads displacement experiments, fluorescent beads (L9529, Sigma-Aldrich) were embedded in collagen at a ratio of 1 : 50 v/v, replacing PLL-*g*-PEG/FITC. Both ends of the flow chamber were sealed with nail polish. Flow chambers with Matrigel were incubated at 37 °C for 40 minutes. Those with collagen were incubated at 37 °C for at least 15 minutes.

Cell viability assay

Madin–Darby canine kidney cells (MDCK.2, CRL-2936, ATCC) were cultured in Dulbecco's modified Eagle's medium (DMEM) (Sigma Aldrich) at 37 °C, 5% CO_2 and 95% humidity at passages bellow 30. Cells were treated with 2 µM calcein-AM (Invitrogen) in serum-free DMEM for 30 minutes and then recovered in DMEM for another 30 minutes. 5 mg mL^{-1} collagen was neutralized with 1 M NaOH and mixed with 200 000 cells and DMEM to achieve a final concentration of 2 mg mL^{-1}. The flow chamber was incubated for at least 1 hour at 37 °C, 5% CO_2, and 95% humidity. Afterwards, 200 µl of 5 µg mL^{-1} propidium iodide (Sigma-Aldrich) in DMEM was added to one inlet of the flow chamber, and imaging was performed at 33 °C and 5% CO_2.

Microscopy

Phase contrast images were acquired using a Nikon Ti-E microscope (Nikon Instruments) (Fig. 2 and 3G).

Bright-field images were obtained using a Nikon Ti2 microscope (Nikon Instruments) equipped with a 20× objective (CFI Plan Fluor 20×, Nikon Instruments) (Fig. 5A and B). A 460 nm LED (power: 259 mW) was used to trigger volume change of the light-responsive hydrogel structures.

Confocal images and *z*-stacks were acquired using a confocal laser scanning microscope (LSM 980, Zeiss) equipped with an 10× objective (Plan-Apochromat 10×/0.45 M27, Zeiss) (Fig. 1, 3A–F and 6). For bead displacement experiments, beads near the edge of a microstructure were imaged every 0.6 seconds within a temperature range from 27 °C to 40 °C (Fig. 4A–C). For spatially selective hydrogel

microstructures contraction (Fig. 5C–E), an area of interest was illuminated with a 561 nm laser.

For the cell viability assay (Fig. 6), sample areas containing microstructures with surrounding cells and areas containing cells but not microstructures were randomly selected for imaging. These areas were imaged using brightfield and confocal fluorescence microscopy. An illumination cycle for actuating the microstructure comprised 40 seconds illumination with a 561 nm laser, followed by 140 recovery.

For Fig. S2, images were acquired using an iPhone 12.

Software for data analysis

Digital masks (TIFF images, 8-bit, 0.27 μm px^{-1}) were designed using the software Inkscape and Fiji.[51]

Hydrogel geometries in phase contrast images were analyzed using Fiji. The analysis to retrieve the area of the imaged microstructures was performed on manually drawn masks along the boundaries of the hydrogel microstructures.

For confocal images, Fiji was used to retrieve the radius of the microstructures. Masks were generated *via* thresholding on the central *z*-stack slice. For bead displacement, the time series were registered using the plugin StackReg and beads were tracked with the TrackMate plugin.[52] To determine cell viability, cells were counted with the 3D Objects Counter.

Origin (OriginLab) and Python were used for plotting and statistical analysis.

Conclusions

In summary, this work presents a novel approach for remodeling biological polymer networks using smart hydrogel microstructures. The expansion and compaction of these hydrogel microstructures were triggered by either light or temperature providing high spatiotemporal control over mechanical perturbations of biological polymer networks, such as collagen and Matrigel. Our approach is well-suited to lab-on-chip applications and cell compatible, with potential future applications including the characterization of diverse extracellular matrix compositions and the mechanical perturbation of cellular systems.

Author contributions

V. S. Q.: conceptualization (supporting); formal analysis (lead); investigation (equal); methodology (equal); writing – original draft (equal); writing – review & editing (equal). K. E.: formal analysis: (supporting); investigation (equal); methodology (equal); writing – original draft (equal); writing – review & editing (supporting). K. Z.: conceptualization (lead); formal analysis (supporting); funding acquisition (lead); methodology (equal); supervision and project administration (lead); writing – original draft (equal); writing – review & editing: (equal).

Conflicts of interest

There are no conflicts to declare.

Data availability

Supplementary information is available. See DOI: **https://doi.org/10.1039/D5LC00477B**.

All data reported in this work are available upon request from the corresponding author upon reasonable request.

Acknowledgements

We thank all members of the Zieske research group for scientific discussions. We thank Matthias Pöllmann and Peter Hull for comments on the manuscript. We acknowledge the core facility "Lab-On-A-Chip" for access to the PRIMO device. Language and grammar of the manuscript was refined with assistance of Chat GPT (v3.5). This work was supported by a Max Planck Research Group grant from the Max Planck society awarded to Katja Zieske. Open Access funding provided by the Max Planck Society.

References

1 T. R. Cox and J. T. Erler, *Dis. Model. Mech.*, 2011, **4**, 165–178.
2 I. T. Swinehart and S. F. Badylak, *Dev. Dyn.*, 2016, **245**, 351–360.
3 R. Agha, R. Ogawa, G. Pietramaggiori and D. P. Orgill, *J. Surg. Res.*, 2011, **171**, 700–708.
4 Y. Wang, J. Y.-J. Shyy and S. Chien, *Annu. Rev. Biomed. Eng.*, 2008, **10**, 1–38.
5 G. Antonacci, T. Beck, A. Bilenca, J. Czarske, K. Elsayad, J. Guck, K. Kim, B. Krug, F. Palombo, R. Prevedel and G. Scarcelli, *Biophys. Rev.*, 2020, **12**, 615–624.
6 S. Kim, M. Uroz, J. L. Bays and C. S. Chen, *Dev. Cell*, 2021, **56**, 180–191.
7 P. Egan, R. Sinko, P. R. LeDuc and S. Keten, *Nat. Commun.*, 2015, **6**, 7418.
8 Z. Zhao, X. Chen, A. M. Dowbaj, A. Sljukic, K. Bratlie, L. Lin, E. L. S. Fong, G. M. Balachander, Z. Chen, A. Soragni, M. Huch, Y. A. Zeng, Q. Wang and H. Yu, *Nat. Rev. Methods Primers*, 2022, **2**, 1–21.
9 J. B. Kim, *Semin. Cancer Biol.*, 2005, **15**, 365–377.
10 C. M. Leung, P. de Haan, K. Ronaldson-Bouchard, G.-A. Kim, J. Ko, H. S. Rho, Z. Chen, P. Habibovic, N. L. Jeon, S. Takayama, M. L. Shuler, G. Vunjak-Novakovic, O. Frey, E. Verpoorte and Y.-C. Toh, *Nat. Rev. Methods Primers*, 2022, **2**, 1–29.
11 R. Joshi, S.-B. Han, W.-K. Cho and D.-H. Kim, *Biomater. Res.*, 2022, **26**, 43.
12 F. Abbasi, K. Rieck, M. Brandt, M. Matis and T. Betz, *bioRxiv*, 2023, preprint, 08.22.554088, DOI: **10.1101/2023.08.22.554088**.
13 C. J. Bustamante, Y. R. Chemla, S. Liu and M. D. Wang, *Nat. Rev. Methods Primers*, 2021, **1**, 1–29.
14 X. Peng and H. Wang, *J. Polym. Sci., Part B: Polym. Phys.*, 2018, **56**, 1314–1324.
15 C. Tsitsilianis, *Soft Matter*, 2010, **6**, 2372–2388.

16 H. L. Lim, Y. Hwang, M. Kar and S. Varghese, *Biomater. Sci.*, 2014, **2**, 603–618.
17 B. Özkale, R. Parreira, A. Bekdemir, L. Pancaldi, E. Özelçi, C. Amadio, M. Kaynak, F. Stellacci, D. J. Mooney and M. S. Sakar, *Lab Chip*, 2019, **19**, 778–788.
18 A. N. Ramey-Ward, Y. Dong, J. Yang, H. Ogasawara, E. C. Bremer-Sai, O. Brazhkina, C. Franck, M. Davis and K. Salaita, *ACS Biomater. Sci. Eng.*, 2023, **9**, 5361–5375.
19 A. Sutton, T. Shirman, J. V. I. Timonen, G. T. England, P. Kim, M. Kolle, T. Ferrante, L. D. Zarzar, E. Strong and J. Aizenberg, *Nat. Commun.*, 2017, **8**, 14700.
20 Y. Chandorkar, A. Castro Nava, S. Schweizerhof, M. Van Dongen, T. Haraszti, J. Köhler, H. Zhang, R. Windoffer, A. Mourran, M. Möller and L. De Laporte, *Nat. Commun.*, 2019, **10**, 4027.
21 S. Khetan and J. A. Burdick, *Soft Matter*, 2011, **7**, 830–838.
22 A. Balena, M. Bianco, F. Pisanello and M. De Vittorio, *Adv. Funct. Mater.*, 2023, **33**, 2211773.
23 M. Kang, C. Han and H. Jeon, *Optica*, 2020, **7**, 1788–1795.
24 J. Rühe, *ACS Nano*, 2017, **11**, 8537–8541.
25 W. J. Polacheck, R. Li, S. G. M. Uzel and R. D. Kamm, *Lab Chip*, 2013, **13**, 2252–2267.
26 T. S. Wilems, X. Lu, Y. E. Kurosu, Z. Khan, H. J. Lim and L. A. Smith Callahan, *J. Biomed. Mater. Res., Part A*, 2017, **105**, 3059–3068.
27 K. Esch and K. Zieske, *bioRxiv*, 2025, preprint, 01.29.635555, DOI: **10.1101/2025.01.29.635555**.
28 A. S. Huffman, A. Afrassiabi and L. C. Dong, *J. Controlled Release*, 1986, **4**, 213–222.
29 Y. Hirokawa and T. Tanaka, *AIP Conf. Proc.*, 1984, **107**, 203–208.
30 C. Wu and X. Wang, *Phys. Rev. Lett.*, 1998, **80**, 4092–4094.
31 H. Cheng, L. Shen and C. Wu, *Macromolecules*, 2006, **39**, 2325–2329.
32 A. K. Velichko, E. N. Markova, N. V. Petrova, S. V. Razin and O. L. Kantidze, *Cell. Mol. Life Sci.*, 2013, **70**, 4229–4241.
33 I. Watanabe and S. Okada, *J. Cell Biol.*, 1967, **32**, 309–323.
34 M. Aliabouzar, C. D. Davidson, W. Y. Wang, O. D. Kripfgans, R. T. Franceschi, A. J. Putnam, J. B. Fowlkes, B. M. Baker and M. L. Fabiilli, *Soft Matter*, 2020, **16**, 6501–6513.
35 S. Maji, M. Aliabouzar, C. Quesada, A. Chiravuri, A. Macpherson, A. Pinch, K. Kazyak, Z. Emara, B. A. Abeid, R. N. Kent, F. S. Midekssa, M. Zhang, B. M. Baker, R. T. Franceschi and M. L. Fabiilli, *Bioact. Mater.*, 2025, **43**, 82–97.
36 G. Benton, I. Arnaoutova, J. George, H. K. Kleinman and J. Koblinski, *Adv. Drug Delivery Rev.*, 2014, **79–80**, 3–18.
37 J. Reed, W. J. Walczak, O. N. Petzold and J. K. Gimzewski, *Langmuir*, 2009, **25**, 36–39.
38 E. Méhes, B. Biri-Kovács, D. G. Isai, M. Gulyás, L. Nyitray and A. Czirók, *PLoS Comput. Biol.*, 2019, **15**, e1007431.
39 S. Nam, J. Lee, D. G. Brownfield and O. Chaudhuri, *Biophys. J.*, 2016, **111**, 2296–2308.
40 D. Rüdiger, K. Kick, A. Goychuk, A. M. Vollmar, E. Frey and S. Zahler, *Cell Rep.*, 2020, **32**, 108015.
41 J. Chang and O. Chaudhuri, *J. Cell Biol.*, 2019, **218**, 2456–2469.
42 E. Rezvani Ghomi, N. Nourbakhsh, M. Akbari Kenari, M. Zare and S. Ramakrishna, *J. Biomed. Mater. Res., Part B*, 2021, **109**, 1986–1999.
43 A. J. Licup, S. Münster, A. Sharma, M. Sheinman, L. M. Jawerth, B. Fabry, D. A. Weitz and F. C. MacKintosh, *Proc. Natl. Acad. Sci. U. S. A.*, 2015, **112**, 9573–9578.
44 E. Ban, J. M. Franklin, S. Nam, L. R. Smith, H. Wang, R. G. Wells, O. Chaudhuri, J. T. Liphardt and V. B. Shenoy, *Biophys. J.*, 2018, **114**, 450–461.
45 J. Kim, J. Feng, C. A. R. Jones, X. Mao, L. M. Sander, H. Levine and B. Sun, *Nat. Commun.*, 2017, **8**, 842.
46 A. M. Stein, D. A. Vader, D. A. Weitz and L. M. Sander, *Complexity*, 2011, **16**, 22–28.
47 K. A. Jansen, A. J. Licup, A. Sharma, R. Rens, F. C. MacKintosh and G. H. Koenderink, *Biophys. J.*, 2018, **114**, 2665–2678.
48 L. Liang, C. Jones, S. Chen, B. Sun and Y. Jiao, *Phys. Biol.*, 2016, **13**, 066001.
49 R. C. Arevalo, J. S. Urbach and D. L. Blair, *Biophys. J.*, 2010, **99**, L65–L67.
50 F. G. Downs, D. J. Lunn, M. J. Booth, J. B. Sauer, W. J. Ramsay, R. G. Klemperer, C. J. Hawker and H. Bayley, *Nat. Chem.*, 2020, **12**, 363–371.
51 J. Schindelin, I. Arganda-Carreras, E. Frise, V. Kaynig, M. Longair, T. Pietzsch, S. Preibisch, C. Rueden, S. Saalfeld, B. Schmid, J.-Y. Tinevez, D. J. White, V. Hartenstein, K. Eliceiri, P. Tomancak and A. Cardona, *Nat. Methods*, 2012, **9**, 676–682.
52 J.-Y. Tinevez, N. Perry, J. Schindelin, G. M. Hoopes, G. D. Reynolds, E. Laplantine, S. Y. Bednarek, S. L. Shorte and K. W. Eliceiri, *Methods*, 2017, **115**, 80–90.